Noname manuscript No.
(will be inserted by the editor)

Induced and tunable multistability due to nonholonomic constraints

Colin Rodwell · **Phanindra Tallapragada**

Received: date / Accepted: date

Abstract *Multistability is an area of interest in robotics and locomotion because the ability to achieve multiple configurations or generate multiple gaits allows a single robotic or mechanical system to perform versatile tasks. This multistability is often achieved by adding multistable elements to the system. However, this work finds that two bodies pinned together with a linear rotational spring can exhibit multistable behavior with the introduction of a nonholonomic constraint. Multistable fixed points of the unforced and undamped system are found to correspond to multistable limit cycles with the introduction of damping and periodic forcing, some of which result in fast net turning. This finding has potential implications in understanding the sharp turns executed by biological swimmers, and could be exploited to perform efficient turns in low degree of actuation robots.*

Keywords Bistability · Nonholonomic Constraints · Locomotion

1 Introduction

Mechanical systems with two or more stable configurations are of increasing interest in soft robotics from the perspective of generating gaits and locomotion, stabilization, and manipulation [1–3]. The general approach to achieve multistability in mechanical systems is to design a potential energy function for the system that has multiple local minima. Each of the minima of the potential function represents a stable configuration and the system's state can transition from one potential minimum to another under certain mechanical actuation. Much of the research has focused on two means to achieve a multi-well potential function: either by designing a system with geometric nonlinearities or by using materials or elastic elements with intrinsic or material nonlinearities. A variety of compliant systems and soft robotic systems possess one or both types of nonlinearities [1, 3–6].

In this paper we forego both of the above approaches and instead show that it is possible for a mechanical system whose associated potential energy has a single well to perform multiple unique stable limit cycle oscillations under the same periodic excitation. Motivated by the rich history of the use of pseudo-rigid body models of continuum and soft mechanical systems [7–11, 11–13], we base our investigation on a planar system with two rigid bodies connected by a linear torsional spring. Specifically, we consider the example of a four degree of freedom planar system with one nonholonomic constraint that is subjected to an internal periodic torque generated between the bodies. This mechanical system is a variation of the Chaplygin sleigh [14–18], a well known nonholonomic system. In earlier works [19] it was shown that a similar idealized version of this system in the absence of any damping, frictional resistance, or forcing has multiple stable configurations that arise from the nonlinear torsional spring or could demonstrate chaotic motion [20] in the absence of any spring connecting the two bodies.

In this paper we show that when damping is introduced into this system, along with periodic forcing, limit cycles in reduced velocity space are produced. We show that depending on the amplitude and frequency of the applied torque, the state of the system can oscillate around different mean states. The feature of tunable multistability that is demonstrated here is not merely one of possessing multiple stable static configurations, but is of a more dynamic nature. When subjected to periodic excitation the system has multiple stable limit cycles in its reduced state space, and depending on which limit cycle the system's state switches to, the motion of the body can be qualitatively different: in one case

---

Colin Rodwell
E-mail: crodwel@g.clemson.edu

Phanindra Tallapragada
E-mail: ptallap@clemson.edu

the mean path of the body is a straight line, while in the other it moves along a circular arc. We thus show gait selection that is determined by switching between limit cycles governed by the interplay of the nonholonomic constraint and the periodic forcing. Such interaction between nonholonomic constraints and periodic excitation has received less attention from the robotics perspective. It has however been investigated in the context of a spherical bearings such as for support of long span bridges, ball vibration absorbers. For instance [21, 22] investigated the problem of a ball rolling in a spherical cavity subjected to parametric excitation and showed rich variety of dynamics, limit cycles and quasi-periodic motion depending on the damping and the excitation parameters.

The results in this paper have applications to mobile soft robots which, by the nature of their interaction with the ground or a substrate, can be subject to nonholonomic constraints. Designing soft robots which exploit such constraints on their dynamics can open up a new means to achieve the properties of multistable mechanical systems. This work also has potential significance to the design and control of swimming robots; in previous work it was demonstrated that nonholonomic constraints are present in the swimming motion of fish-like bodies [23–25] and this recognition can enable the design of better controllers for swimming robots [25–28]. The results in this paper show the possibility of achieving different stable limit cycles in physically different configurations and associated gaits for swimming robots without changing the input forcing, which can greatly improve their agility. Within the context of nonholonomic systems, which is a very well studied topic [16, 29–32] in mechanics and robotics, the findings in this paper show the importance of periodic excitation in producing a variety of gaits.

The paper is organized as follows. In section 2 the model of Chaplygin sleigh with an additional appendage and the governing equations of motion are discussed and their relation to previous work is reviewed. In section 3.1 the special case of a non dissipative and unforced Chaplygin sleigh with an elastic appendage is discussed. The fixed points for velocity of the undamped, unforced sleigh exist as shown in [19].The undamped unforced case bears significance to the damped and periodically forced Chaplygin sleigh; although these fixed points disappear for the damped and forced sleigh, limit cycles are produced around them. The stability and bifurcations of these limit cycles and their relevance to the physical gaits of the Chaplygin sleigh are discussed in section 3.

2 Mechanical model and governing equations

The Chaplygin sleigh is a rigid body with a knife edge at one end that prevents slipping in the transverse direction as it moves in a plane. This no-slip condition is a nonholonomic constraint, and this seemingly simple mechanical system can exhibit very rich dynamics [14–18, 33, 34]. In this paper we consider a modified two-link Chaplygin sleigh as depicted in fig. 1. The rear link of length εl will be referred to as the "tail", and it is connected to the other link (referred to as the "head" link) at a revolute joint with a linear torsional spring of constant stiffness K. The two link Chaplygin sleigh is motivated by potential applications to fish-like swimming robots as well as the multi-link snake-like terrestrial robots. The torsional spring at the revolute joint mimics the stiffness of the tail of a fish or a reptile. The spatial frame is denoted by $X-Y$, and the body frame denoted by X_b-Y_b is attached to the tail link with its origin collocated with the revolute joint. The tail link has a massless wheel or a knife edge at its end which prevents slipping in the transverse (Y_b) direction but allows motion in the longitudinal (X_b) direction.

The configuration space of the system is $Q = SE2\times S^1$ and is parameterized by the coordinates $\boldsymbol{q} = (x_1, y_1, \theta_1, \theta_2)$ where (x_1, y_1) are the coordinates of the center of mass of the sleigh tail link, θ_1 is the angle made by the body frame with respect to the spatial frame and θ_2 is the angle of the vector between the revolute joint and the center of mass of the head link with respect to the spatial frame. The Lagrangian of the system is $\mathscr{L} = \mathscr{T}(\boldsymbol{q},\dot{\boldsymbol{q}}) - \mathscr{V}(\boldsymbol{q})$ with kinetic energy $\mathscr{T} = \frac{1}{2}\dot{\boldsymbol{q}}^T\mathscr{M}(\boldsymbol{q})\dot{\boldsymbol{q}}$ and potential energy $\mathscr{V}(\boldsymbol{q}) = \frac{1}{2}K\delta^2$. It is emphasized that K is taken as a constant, so the potential function is a single-well potential and does not by itself produce multiple equilibria. The mass matrix $\mathscr{M}$ is defined in the appendix. We imagine that a motor at the revolute joint applies an internal periodic torque $A\sin\Omega t$, which results in equal and opposite torques on the head and tail links. The resulting spin and translation of the tail link has to satisfy the nonholonomic constraint, which defines that transverse velocity u_y (along the Y_b direction) of the point P is constrained to be zero,

$$u_y = -\sin\theta_1\,\dot{x}_1 + \cos\theta_1\,\dot{y}_1 - \varepsilon\, l\,\dot{\theta}_1 = 0. \tag{1}$$

The constraint can be expressed compactly as $\mathscr{W}(\boldsymbol{q})\dot{\boldsymbol{q}} = 0$ with $\mathscr{W}(\boldsymbol{q}) = [-\sin\theta\ \cos(\theta)\ -\varepsilon l\ 0]$.

We further assume that the sleigh experiences viscous dissipation with the Rayleigh function

$$\mathscr{R} = \frac{1}{2}\left(c_u(\dot{x}_1\cos\theta_1 + \dot{y}_1\sin\theta_1)^2 + c_\omega\dot{\theta}_1{}^2 + c_\delta\dot{\delta}^2\right), \tag{2}$$

where $\delta = \theta_2 - \theta_1$ and c_u, c_θ, and c_δ refer to the damping on the translational velocity at the constraint, the rotational velocity of the tail link, and the interlink rotational velocity, respectively. The Euler-Lagrange equations with the constraint forces are

$$\begin{bmatrix} \mathscr{M} & -\mathscr{W}^T \\ \mathscr{W} & 0 \end{bmatrix}\begin{bmatrix} \ddot{\boldsymbol{q}} \\ \lambda \end{bmatrix} = \begin{bmatrix} \mathscr{B}(\boldsymbol{q},\dot{\boldsymbol{q}}) \\ -\dot{\mathscr{W}}\dot{\boldsymbol{q}} \end{bmatrix} + \left[\boldsymbol{\tau}(t)\right]. \tag{3}$$

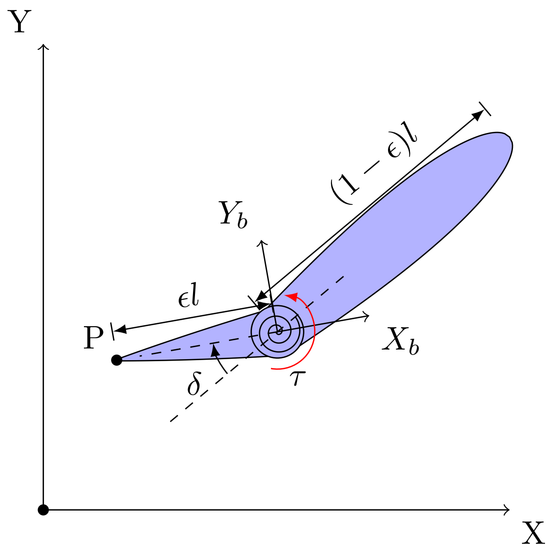

Fig. 1 A two link Chaplygin sleigh system of total length l and total mass m. The tail link of length εl, mass m_1, and moment of inertia I_1 and the head link of mass m_2 and moment of inertia I_2 are connected by a revolute joint. The body frame $X_b - Y_b$ is fixed to the revolute joint and the X_b axis is aligned with the tail longitudinal axis. The velocity of the point P on the tail link is constrained to be zero in the Y_b direction. The angle θ_1 is the angle between the body frame and the spatial frame while angle δ is the relative angle between the links, and $\delta = 0$ corresponds to the fully extended configuration. The center of mass of the tail link is along the line joining P to the revolute joint. The center of mass of the head link is at a distance of $\frac{l}{2}(1-\varepsilon)$ from the joint and the special case where the head link length is $l(1-\varepsilon)$ is considered.

The forcing term is $\boldsymbol{\tau}$ and the only non-zero forcing terms are the joint torque $\boldsymbol{\tau}_3 = -\boldsymbol{\tau}_4 = A\sin\Omega t$. The vector $\mathscr{B}(\boldsymbol{q},\dot{\boldsymbol{q}})$ contains the gyroscopic terms and the elastic forces, the ith entry of which is

$$\mathscr{B}_i = \frac{1}{2}\left(\frac{\partial \mathscr{M}_{ik}}{\partial \boldsymbol{q}^j} + \frac{\partial \mathscr{M}_{ji}}{\partial \boldsymbol{q}^k} - \frac{\partial \mathscr{M}_{jk}}{\partial \boldsymbol{q}^i}\right)\dot{\boldsymbol{q}}^j\dot{\boldsymbol{q}}^k - \frac{\partial \mathscr{V}}{\partial \boldsymbol{q}^i} - \frac{\partial \mathscr{R}}{\partial \dot{\boldsymbol{q}}^i}$$

The resulting Euler-Lagrange equations are independent of (x,y,θ_1) and a reduction of the equations to the body frame creates a reduced system of velocity equations decoupled from the grouped variables (x,y,θ_1). Setting $\boldsymbol{\xi} = [u_x,\omega_1,\omega_2,\delta]^T$ where u_x is the velocity at the constraint, $\omega_1 = \dot{\theta}_1$, and $\omega_2 = \dot{\delta}$, the velocities can be transformed to the body frame as

$$\begin{bmatrix}\dot{x}\\ \dot{y}\end{bmatrix} = \mathbf{R}\begin{bmatrix}u_x\\ 0\end{bmatrix} \quad \text{and} \quad \begin{bmatrix}\ddot{x}\\ \ddot{y}\end{bmatrix} = \mathbf{R}\begin{bmatrix}\dot{u}_x\\ 0\end{bmatrix} + \omega_1 \times \mathbf{R}\begin{bmatrix}u_x\\ 0\end{bmatrix} \tag{4}$$

for rotation matrix $\mathbf{R}(\theta)$. Note that (x_1,y_1) denote the position of the center of mass of the tail link, and (x,y) denote the position of the constraint.

While the derivation to this point is applicable for arbitrary geometry, for our analysis we will consider a specific geometry where both links are rectangular with total width $\frac{l}{2}$, moment of inertia coefficient $\gamma = 1/12$ and constant density. In this case the mass and inertia parameters of the links defined in the caption of fig. 1 can be defined in terms of the geometric parameters and overall mass defined in the same figure as $m_1 = \frac{\varepsilon l}{m}$, $m_2 = \frac{(1-\varepsilon)l}{m}$, $I_1 = 4\gamma m_1\left((\varepsilon l)^2 + \frac{l^2}{4}\right)$ and $I_2 = 4\gamma m_2\left(((1-\varepsilon)l)^2 + \frac{l^2}{4}\right)$. The variables and parameters are then rescaled to eliminate m and l by defining $u_x' = \frac{u_x}{l}$, $A' = \frac{A}{ml^2}$, $\alpha = \sqrt{\frac{K}{ml^2}}$, $c_u' = \frac{c_u}{m}$, $c_\omega' = \frac{c_\omega}{ml^2}$, $c_\delta' = \frac{c_\delta}{ml^2}$, $I_1' = \frac{I_1}{ml^2}$, $I_2' = \frac{I_2}{ml^2}$, $m_1' = \frac{m_1}{m}$, and $m_2' = \frac{m_2}{m}$. A new variable E' representing the rescaled energy is introduced as $E' = \frac{E}{ml^2}$ where $E = \mathscr{T} + \mathscr{V}$. As a further simplification, we consider the rescaled damping ratios equal, so $c = c_u = c_\theta = c_\delta$, and rescaled stiffness α is taken to be $\sqrt{10}$ throughout the paper. For simplicity of notation, the $'$ superscripts are dropped, and all instances of the redefined constants henceforth are taken to be in their scaled form, unless noted otherwise.

The rescaled equations of motion are of the form

$$\mathscr{N}\dot{\boldsymbol{\xi}} = \boldsymbol{g}(\boldsymbol{\xi}) + \boldsymbol{f}(t), \tag{5}$$

where the rescaled inertia-like matrix $\mathscr{N}(\boldsymbol{\xi})$ is described by (16) in the appendix. The four entries of the vector field $\boldsymbol{g} \in \mathbb{R}^4$ are

$$\begin{aligned}\boldsymbol{g}_1 = {} & (\omega_1+\omega_2)^2(\varepsilon-1)^2\cos\delta + (2-\varepsilon)\varepsilon\omega_1^2 \\ & - c_u u_x\end{aligned} \tag{6}$$

$$\begin{aligned}\boldsymbol{g}_2 = {} & 2\varepsilon\omega_2(2\omega_1+\omega_2)(\varepsilon-1)^2\sin\delta \\ & - \omega_1 u_x(\varepsilon-1)^2\cos\delta + (\varepsilon-2)\omega_1 u_x\varepsilon - c_\omega\omega_1\end{aligned} \tag{7}$$

$$\begin{aligned}\boldsymbol{g}_3 = {} & -\omega_1 u_x(\varepsilon-1)^2\cos\delta - 2\omega_1^2\varepsilon(\varepsilon-1)^2\sin\delta \\ & - \alpha^2\delta - \omega_2 c_\delta\end{aligned} \tag{8}$$

and

$$\boldsymbol{g}_4 = \omega_2. \tag{9}$$

The forcing term $\boldsymbol{f}(t)$ is periodic with frequency Ω,

$$\boldsymbol{f}(t) = \begin{bmatrix}0\\ 0\\ A\sin\Omega t\\ 0\end{bmatrix}. \tag{10}$$

3 Tunable limit cycles and configuration changes

The periodically forced two-link Chaplygin sleigh demonstrates complex dynamics that depend on the frequency and amplitude of the forcing as well as geometric parameters such as ε. Underlying this behavior are dynamics of the unforced and non-dissipative two-link Chaplygin sleigh system. This is a general theme in many dynamical systems, such as the multi-well Duffing oscillator, where the fixed points of the unforced Duffing oscillator form the skeleton of the dissipative forced dynamics. Therefore we first discuss the somewhat simpler case of the dynamical system with no dissipation and free of forcing, i.e. $c = 0$ and $\boldsymbol{f}(t) = \mathbf{0}$.

3.1 Multistability in the conservative system

Suppose $\boldsymbol{h}(\boldsymbol{\xi}) = \boldsymbol{g}(\boldsymbol{\xi}; c_u = 0, c_\omega = 0, c_\delta = 0, A = 0)$: it will be shown that the limit cycles of interest of the dynamical system (5) are created around the fixed points of the dynamical system

$$\mathscr{N}\dot{\boldsymbol{\xi}} = \boldsymbol{h}(\boldsymbol{\xi}). \tag{11}$$

One observation that can be made about the dynamical system (11) is that the total energy $E = \mathscr{T} + \mathscr{V}$ is constant along its integral curves in the absence of any damping or forcing. The inertia tensor $\mathscr{N}$ is symmetric and positive definite and thus invertible except at $\varepsilon = 1$. The fixed points of (11) are therefore given by $\mathscr{N}^{-1}\boldsymbol{h}(\boldsymbol{\xi}) = \mathbf{0}$, and since the determinant $\det(\mathscr{N}) \neq 0$, the only solution to this is $\boldsymbol{h}(\boldsymbol{\xi}) = \mathbf{0}$. The fixed points of (11) are non-isolated due to the conservation of energy; a continuous family of fixed points exists as the energy of the system is varied, and perturbations from a fixed point that change the energy of the system can never decay to the same fixed point. To isolate the fixed points, we perform a reduction of dimension of (11) by considering dynamics restricted to a constant energy manifold. This reduced dynamical system denoted by $\dot{\boldsymbol{\xi}}_r = \boldsymbol{H}_r(\boldsymbol{\xi}_r; E)$ is described in the appendix (27) where $\boldsymbol{\xi}_r = [\omega_1, \omega_2, \delta]^T$ and the longitudinal velocity denoted as a function of $\boldsymbol{\xi}_r$ as $u_x = u_x(\boldsymbol{\xi}_r; E)$. We will then consider perturbations around a fixed point that preserve energy.

This system has two distinct types of fixed points. It can be verified that $(u_x = \pm\sqrt{2E}, \omega_1 = 0, \omega_2 = 0, \delta = 0)$ is one set of fixed points. This set of fixed points corresponds to straight line motion where the sleigh shape is straight with $\delta = 0$; the sleigh could be moving forward $\left(u_x = \sqrt{2E}\right)$ or backward $\left(u_x = -\sqrt{2E}\right)$. The Jacobian $\mathbf{J}$ is the gradient of the reduced vector field $\boldsymbol{H}_r(\boldsymbol{\xi}_r; E)$. The eigenvalues of $\boldsymbol{J}$, denoted by (μ_1, μ_2, μ_3) in descending order of their real component, are in the left half plane when evaluated for fixed points corresponding to $u_x = \sqrt{2E}$ as shown in fig. 2 and in the right half plane for fixed points corresponding to $u_x = -\sqrt{2E}$ [19].

The other set of fixed points corresponds to a buckled shape with $\delta = \pm\delta^*$ (symmetrically placed to the "left" and "right" of the longitudinal axis of the tail link) where

$$\delta^* = \cos^{-1}\left(\frac{\varepsilon\,(\varepsilon - 2)}{\varepsilon^2 - 2\,\varepsilon + 1}\right) \tag{12}$$

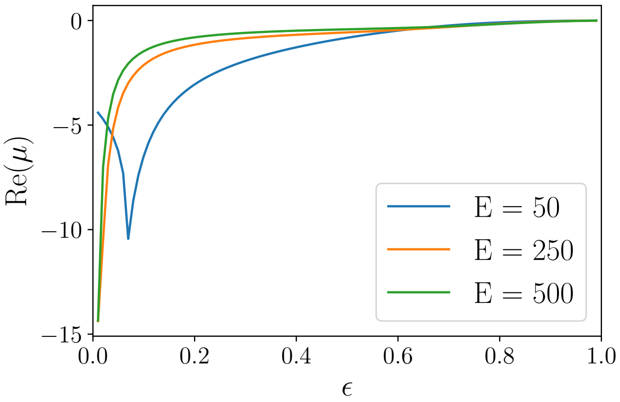

Fig. 2 The largest real component of the eigenvalues of the Jacobian $\boldsymbol{J}$ about the forward non-buckled fixed point $(u_x = \sqrt{2E}, \omega_1 = 0, \omega_2 = 0, \delta = 0)$ for varying energies with $\varepsilon = 0.15$, $c = 0$, and $A = 0$. The real component of the largest eigenvalue, and thus all the eigenvalues, is always negative, indicating that the non-buckled fixed points with positive u_x are always stable within the considered energy range $0 < E < 1000$.

is obtained from solving (7) $\boldsymbol{g}_1 = 0$ or $\boldsymbol{g}_2 = 0$. The buckled fixed points exist only if $\varepsilon < \varepsilon_0 = 1 - \frac{1}{\sqrt{2}}$. For each of the $\pm\delta^*$ there exist at most four pairs of ω_1^* and u_x^* which satisfy $\dot{\boldsymbol{\xi}} = 0$ for a given energy level. The values of u_x^* and ω_1^* are given in (28) and (29) in the appendix. All four fixed points exist for $\varepsilon_l < \varepsilon < \varepsilon_0$, where ε_l is a function of energy, with sample values shown in fig. 3. There are thus a total of eight fixed points for the buckled state of motion. The four values of u_x^* and ω_1^* corresponding for each of the symmetric shapes $\pm\delta^*$ imply that at each of the symmetric equilibrium shapes, the kinetic energy of the system can be partitioned into two possible values of translational and rotational energies. Because these energies can result in either forward or backwards motion, for the two fixed points in positive u_x, (u_x^*, ω_1^*), the two pairs $-(u_x^*, \omega_1^*)$ are also fixed points. Numerical evaluation of the eigenvalues of the Jacobian, $\boldsymbol{J}(\omega_1^*, \omega_2 = 0, \delta^*, E)$ show that only of one of these partitions of energy is stable, so there are two stable and six unstable equilibrium states of motion in the buckled state. For reasons of symmetry, we show results of these simulations only for the buckled state with $\delta = +\delta^*$ and the same result holds for the other buckled state $\delta = -\delta^*$. Fig. 3 shows a plot of the variation of the fixed points (u_x^*, ω_1^*) as the bifurcation parameter ε varies for different energies E of the system. The portion of the curves shown by solid lines represent the stable fixed points and the dashed lines represent the unstable fixed points.

Fig. 4 shows a plot of the eigenvalues of the Jacobian $\boldsymbol{J}(\omega_1^*, \omega_2 = 0, \delta^*, E)$ with the largest real component evaluated at the stable and unstable fixed points with positive u_x. For the stable fixed point, the eigenvalues with the highest real part, shown by blue solid lines for different values of E, are in the left half plane, with the exception of a small region

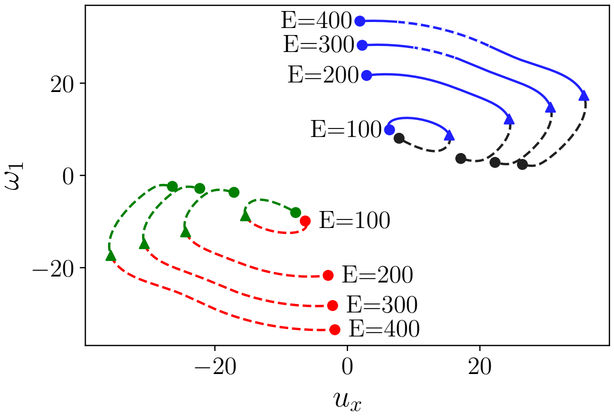

Fig. 3 Dependence of the locations of fixed points u_x^* and ω_1^* on ε for a sampling of energy levels for the conservative system. Circles indicate $\varepsilon = 1 - \frac{1}{\sqrt{2}}$, the maximum ε value for which $\delta^* \neq 0$ fixed points exist. The fixed point locations then vary with decreasing ε until their annihilation at $\varepsilon_l(E)$, indicated by triangular markings. The lower bound $\varepsilon_l(E)$, varies with energy, and corresponds to $\varepsilon = 0.134, 0.053, 0.034, 0.025$ for energies $E = (100, 200, 300, 400)$, respectively. Dashed lines indicate unstable fixed points while solid lines indicate stable fixed points.

in the right half plane at high E values. The black solid line shows the highest real eigenvalue of the Jacobian evaluated at the lower ω_1^* fixed point in positive u_x. The eigenvalues start at the upper ε limit ε_0 with a value of $\mu = 0 + 0i$, and as ε decreases the stable fixed points gain a complex component, while the unstable eigenvalues remain on the real axis. As ε decreases further to a critical value ε_l (shown by the triangles in fig. 3), the pairs of fixed points collide and annihilate in a saddle-node bifurcation, and the eigenvalues of J about the four fixed points return smoothly to $\mu = 0 + 0i$. Jacobian matrices calculated about the fixed points in negative u_x^* are found to always have at least one eigenvalue with a positive real component.

3.2 Multistability in the dissipative forced system

With the addition of damping, all the fixed points of the conservative system (11), with the exception of the origin $\boldsymbol{\xi} = [0, 0, 0, 0]^T$, disappear. This can be shown based on the movement of energy into and out of the system, which is given by

$$\frac{dE}{dt} = \left(-c_u u_x^2 - c_\omega \omega_1^2 - c_\delta \omega_2^2 + \omega_2 A \sin \Omega t\right). \tag{13}$$

In the absence of any forcing, $A = 0$, $\dot{E} < 0$ except for the rest state $(u_x = 0, \omega_1 = 0, \omega_2 = 0)$. Furthermore the rest state $\boldsymbol{\xi} = [0, 0, 0, 0]^T$ is a fixed point and it can be checked that $\boldsymbol{g}(\boldsymbol{\xi} = [0, 0, 0, 0]^T) = 0$. Setting E as a Lyapunov function, we can therefore conclude that $\boldsymbol{\xi} = [0, 0, 0, 0]^T$ is a global attractor for this system if spring stiffness is positive.

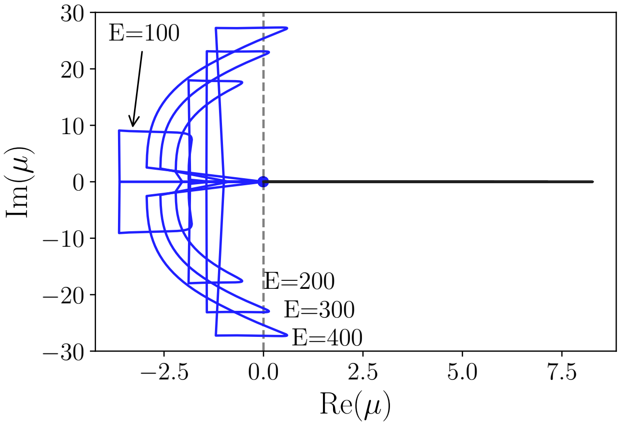

Fig. 4 The eigenvalues with the highest real component of the Jacobian $\boldsymbol{J}$ of positive u_x buckled fixed points of the conservative system shown in fig. 3. Four energy values, $E = 100, 200, 300$, and 400, are selected, and ε is varied between the maximum ε value $\varepsilon_0 = 1 - \frac{1}{\sqrt{2}}$ and the minimum $\varepsilon_l(E)$. The highest eigenvalue of the black curve from fig. 3, which has the lower ω_1^* value in positive u_x, is purely real and never negative. The fixed points for the blue line start at $\mu = 0 + 0i$ at the upper epsilon bound and return there at the lower bound. Between those bounds, the eigenvalues can mostly be found in the left-half plane, indicating stability with the exception of a small ε region at high energies which coincides with the dashed portion of the blue line in fig. 3.

When the forcing $\boldsymbol{f}(t) \neq \boldsymbol{0}$, the origin is no longer a fixed point of (5) since $\boldsymbol{g}(\boldsymbol{\xi}) = 0$ and $\boldsymbol{f}(t) \neq \boldsymbol{0}$. In fact, the periodically forced dynamical system (5) has no fixed points. However, the effect of the "ghost fixed points" of (11) persists in that limit cycles of the dissipative system are created around fixed points of the conservative system. The existence and stability of these limit cycles is dependent on the amplitude and frequency of the forcing torque, making it possible to tune or select the limit cycles of the system in real time. Much like the fixed points of the conservative system, the limit cycles of the forced dissipative system can be broadly classified into two types. The first type features oscillations of the tail where the mean value of the angle δ is zero. A set of such limit cycles are shown in fig. 5(a) in the space of (u_x, ω_1, δ) for varying amplitudes of the forcing torque. As the amplitude of the forcing increases, the amplitude of the oscillations of the tail and of the flexing of the body increase, as does the longitudinal speed u_x. These limit cycles have a slight twist which manifests in the self-intersecting "figure-8" curves that appear when the limit cycles are projected onto the $\omega_1 - u_x$ subspace. These self-intersecting curves indicate that the longitudinal velocity u_x has a fundamental frequency twice that of the angular velocity ω_1, which is reminiscent of similar behavior for a single link Chaplygin sleigh [18].

These small amplitude limit cycle oscillations around the $\delta = 0$ non-buckled configuration lead to a trajectory of the constraint point which is serpentine with small peak-to-peak variation in the physical plane such as shown in fig.

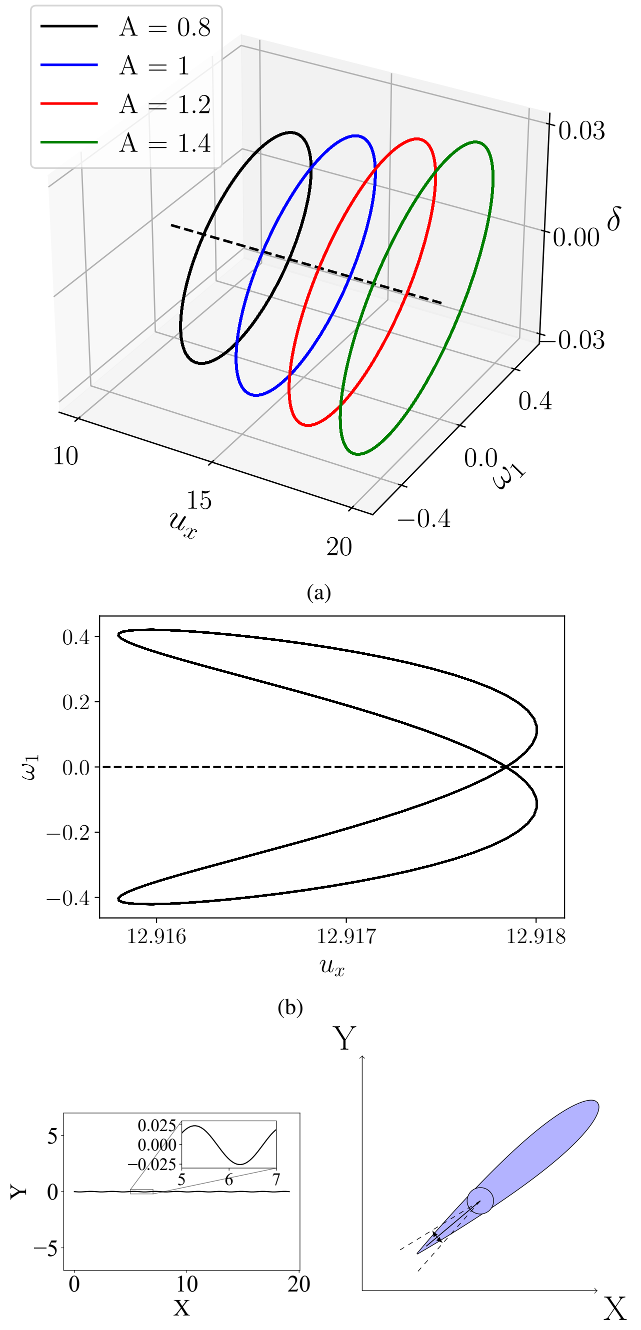

(a)

(b)

(c) (d)

Fig. 5 (a) Limit cycles of the forced dissipative system with $c = 0.001$, $\varepsilon = 0.15$, and $\Omega = 21$ about the $\delta = 0$ fixed points of the conservative system (indicated by a dashed line). These limit cycles take the form of near-circular orbits. The response to increasing forcing amplitude is an increased amplitude of oscillations and increased velocity u_x. (b) A projection of the limit cycle (for $A = 0.8$) onto the u_x-ω_1 plane with two self crossing loops symmetric about $\omega_1 = 0$. (c) The serpentine path of the sleigh with average straight-line motion. (d) Small amplitude oscillations of the tail with the extreme angles δ shown by the dashed lines.

5(c). However, the time averaged (over integer multiples of $T = \frac{2\pi}{\Omega}$) path is a straight line. The amplitude of tail oscillations is small as shown in fig. 5(d). An animation of this motion is shown in the supplementary video.

A different set of stable limit cycles coexist when the forcing frequency Ω is close to a natural frequency of oscillations seen in the conservative system around the buckled fixed points. A natural frequency for this system can be defined as the imaginary component of the eigenvalue with the highest real component, μ_1, of the Jacobian $\boldsymbol{J}$ evaluated at the buckled fixed points of the conservative system. Fig. 6(a) shows limit cycles in the $u_x - \omega_1 - \delta$ space due to a forcing frequency of $\Omega = 21$. This forcing frequency is close to the natural frequency $Im(\mu_1) = 20.8$ of the stable buckled fixed point of the conservative system at $\varepsilon = 0.15$ and $E = 300$. This energy value is roughly representative of the cycles shown in fig. 6(a), which have energies that vary with both time and forcing amplitude, but are bounded between a minimum of $E = 297$ for $A = 0.8$ and a maximum of $E = 317$ for $A = 1.4$. The limit cycles grow in diameter and energy as the amplitude of the forcing increases. Interestingly, the limit cycles are centered around and enclose the locus of the buckled state fixed points of the conservative system, shown by the dashed (magenta) curve. The time-averaged value of ω_1 along these limit cycles is clearly non-zero, and as a result the sleigh moves along a sharply curved path in the $X - Y$ plane as shown in fig. 6(b) with the tail oscillating about the buckled state as shown in fig. 6(c). The supplementary video also shows an animation of this type of gait.

To understand the stability of the limit cycles in the buckled configuration, we analyze the stability of the fixed points of the time T-Poincare map. Suppose the flow map for the dynamical system (5) is $\Phi_{t_0}^{t} : \boldsymbol{\xi}(t_0) \mapsto \boldsymbol{\xi}(t)$. The T-periodic Poincaré map is

$$\mathscr{P} : \boldsymbol{\xi}(t) \mapsto \boldsymbol{\xi}(t+T). \tag{14}$$

Here $T = \frac{2\pi}{\Omega}$ is the time period of the forcing function. Any initial condition on a limit cycle (or any periodic solution) with a fundamental frequency that is an integer multiple of Ω is a fixed point of the Poincaré map $\mathscr{P}$. The stability of a limit cycle is characterized by the stability of the corresponding fixed points of the Poincaré map (14). The Jacobian of $\mathscr{P}$ evaluated at a fixed point $\boldsymbol{\xi}^*$ will be denoted by $\mathbf{J}_p(\boldsymbol{\xi}^*)$ and its eigenvalues by η, and is calculated numerically using finite differences.

The stability of the fixed points of $\mathscr{P}$ depends on the forcing frequency Ω, which acts as a bifurcation parameter. Figure 7(a) shows the magnitude of the eigenvalues of $\mathbf{J}_p(\boldsymbol{\xi}^*)$ for $\boldsymbol{\xi}^*$ on the buckled limit cycle with $A = 1$, and fig. 7(b) shows the same eigenvalues in the complex plane. For these parameters all the eigenvalues of $\mathbf{J}_p(\boldsymbol{\xi}^*)$ are less than one in magnitude for forcing frequency Ω in a small range around 21, specifically between two critical values of the bifurcation parameter $\Omega = 18.71$ and $\Omega = 24.65$. At these

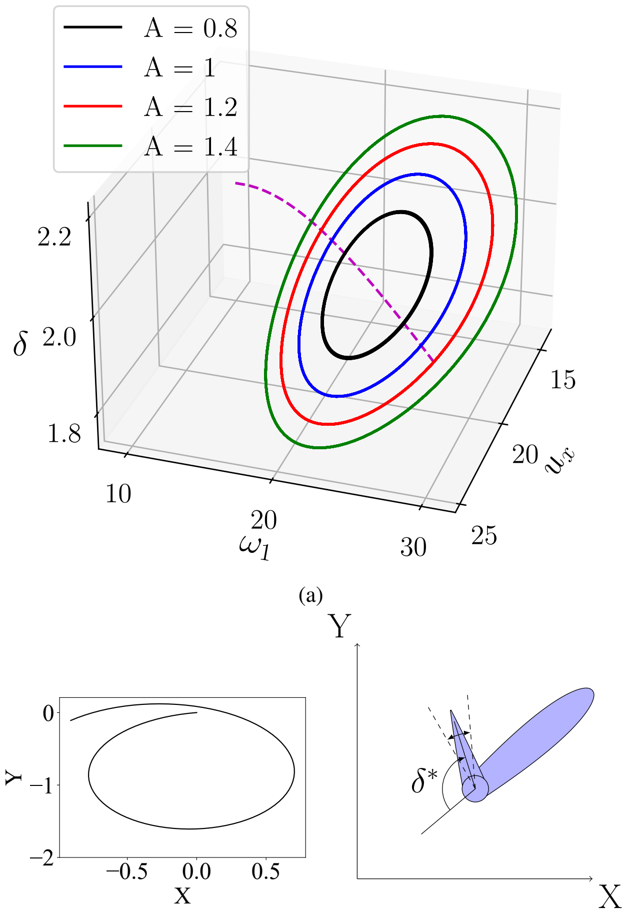

(a)

(b)

(c)

Fig. 6 (a) The limit cycles of the dissipative system at varying forcing amplitudes, with constant damping $c = 0.001$, forcing frequency $\Omega = 21$, and $\varepsilon = 0.15$. The locus of stable fixed points of the conservative system as energy varies energy pass through the dissipative limit cycles. Due to symmetry, an identical set of fixed points and limit cycles exists reflected about $\delta = 0$ and $\omega_1 = 0$, corresponding to turning in the other direction. (b) The path traced by the constraint point over a single forcing period, indicating fast turning motion along curved paths with the limit cycle oscillations about the buckled tail configuration. (c) The small amplitude of interlink oscillations are shown by the dashed lines around the buckled state.

critical frequencies one of the eigenvalues crosses the unit circle along the real axis. Beyond these critical values, the limit cycle becomes unstable and adjacent trajectories are repelled and instead converge to the limit cycle around the non-buckled $\boldsymbol{\xi} = [u_x, 0, 0, 0]^T$ state as show in fig. 8. This bifurcation behavior invites the possibility of tuning Ω to attract or repel trajectories from certain limit cycles. Numerical simulations show that this switchable multistability that depends on the forcing frequency Ω exists for a large range of forcing amplitudes and frequencies.

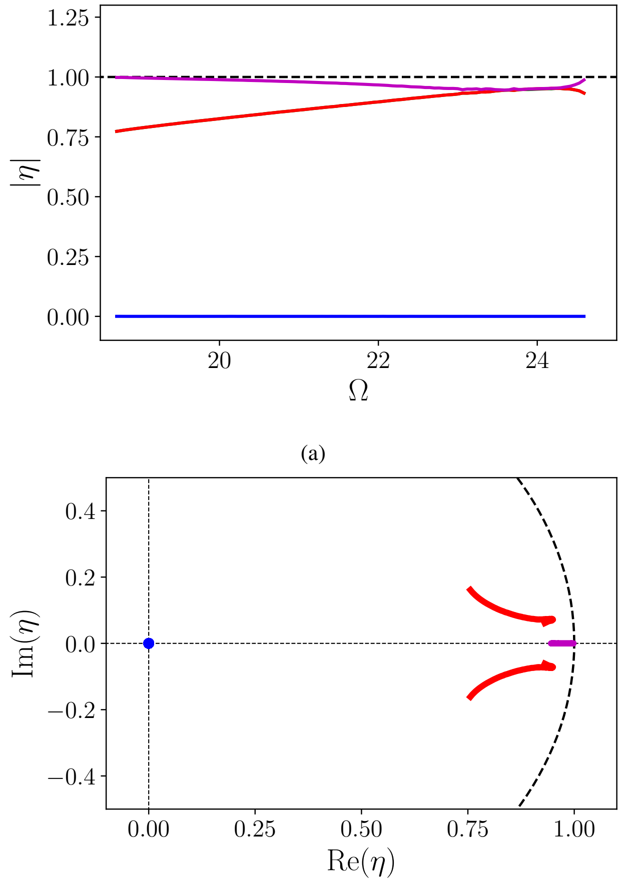

(a)

(b)

Fig. 7 The eigenvalues η of the T-periodic Poincaré map of the forced and dissipative system performing limit cycle oscillations with varied forcing frequency Ω in a turning gait with $A = 1$, $\varepsilon = 0.15$, and $c = 0.001$. Subfigure (a) shows the evolution of the eigenvalues of the Jacobian about the fixed point with varying Ω, and (b) shows the eigenvalue trajectories in the complex plane for the same range of Ω. Bifurcations at $\Omega = 18.71$ and $\Omega = 24.65$ bound a range of forcing frequency which leads to stable limit cycles around the buckled state. Outside of this range, all tested initial conditions were found to converge to straight-motion limit cycles.

4 Conclusion

This paper demonstrates that a mobile mechanical system with a nonholonomic constraint and periodic forcing can exhibit multistable limit cycles in a reduced velocity space. This multistability is achieved in the absence a of multi-well elastic potential function and is the result of the nonholonomic constraint. The different limit cycles correspond to different types of motion or gaits in the plane: an averaged straight line motion and a rapid turning motion. Additionally, the stability of some of these limit cycles can be changed in real time by changing forcing parameters such as the frequency, so switching between gaits can be achieved by controlling the forcing frequency. The significance of these findings is that tunable multistability can be achieved

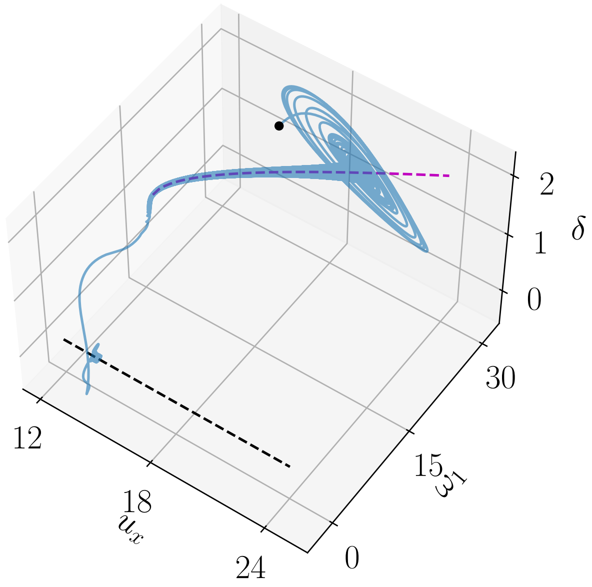

Fig. 8 A trajectory with $A = 1$, $\Omega = 25$, $\varepsilon = 0.15$ and $c = 0.001$, corresponding to slightly above the upper Ω bound for stable limit cycles derived in fig. 7(a). Starting at initial conditions indicated by a circle, the trajectory is drawn towards the buckled fixed points of the conservative system, represented by a magenta line. However, in contrast to the stable range in fig. 7(a), the oscillations do not provide enough energy to counteract dissipation, and the cycles decay along the fixed point until the fixed point is annihilated in saddle-node bifurcation, at which point it jumps to a non-buckled limit cycle about the $\delta = 0$ fixed point, indicated by a black line.

in mechanical systems using the interplay of nonholonomic constraints and forcing, without the necessity of complex geometric or material nonlinearities. This has important implications for the area of mobile robots, particularly soft robots, where such constraints are often ignored. Such constraints can be designed and exploited to easily induce multistability for manipulation or mobility tasks.

5 Funding

This work was partially supported by the National Science Foundation Grant CMMI 2021612 and Office of Navy Research Grant N00014-20-S-B001.

6 Conflicts of interest/Competing interests

The authors declare that they have no conflict of interest.

7 Availability of data and material

Data sharing not applicable to this article as no datasets were generated or analysed during the current study.

8 Code availability

Python code can be made available upon request.

9 Appendix

The mass matrix used in the Lagrangian and the equation of motion (3) is

$$\mathscr{M} = \begin{bmatrix} m & 0 & -m_2\,\varepsilon\, l\sin\theta_1 & -m_2\,(1-\varepsilon)\, l\sin\theta_2 \\ 0 & m & m_2\,\varepsilon\, l\cos\theta_1 & m_2\,(1-\varepsilon)\, l\cos\theta_2 \\ -m_2\,\varepsilon\, l\sin\theta_1 & m_2\,\varepsilon\, l\cos\theta_1 & m_2\,\varepsilon^2 l^2 + I_1 & m_2\,\varepsilon\,(1-\varepsilon)\, l\cos(\theta_2-\theta_1) \\ -m_2\,(1-\varepsilon)\, l\sin\theta_2 & m_2\,(1-\varepsilon)\, l\cos\theta_2 & m_2\,\varepsilon\,(1-\varepsilon)\, l^2\cos(\theta_2-\theta_1) & m_2\,(1-\varepsilon)^2\, l + I_2 \end{bmatrix}. \tag{15}$$

Note that the mass matrix is used in the derivation before the rescaling, so the parameters here have not been rescaled. In the dynamical system (5) $\mathscr{N}\dot{\boldsymbol{\xi}} = \boldsymbol{g}(\boldsymbol{\xi}) + \boldsymbol{f}(t)$, the inertia-like tensor

$$\mathscr{N} = \begin{bmatrix} 1 & -\sin\delta\,(\varepsilon-1)^2 & -\sin\delta\,(\varepsilon-1)^2 & 0 \\ -\sin\delta\,(\varepsilon-1)^2 & \mathscr{N}_{2,2} & \mathscr{N}_{2,3} & 0 \\ -\sin\delta\,(\varepsilon-1)^2 & \mathscr{N}_{2,3} & \mathscr{N}_{3,3} & 0 \\ 0 & 0 & 0 & 1 \end{bmatrix} \tag{16}$$

where

$$\mathscr{N}_{2,2} = 4\,\varepsilon\,(\varepsilon-1)^2\cos(\delta) - 4\,\varepsilon^3 + (48\,\gamma+7)\varepsilon^2 + (-48\,\gamma-3)\varepsilon + 16\,\gamma + 1 \tag{17}$$

$$\mathscr{N}_{2,3} = -(\varepsilon-1)(16\,\varepsilon^2\gamma - 2\,\varepsilon^2\cos(\delta) - 32\,\varepsilon\,\gamma + 2\,\varepsilon\cos(\delta) + \varepsilon^2 + \gamma r^2 + 16\,\gamma - 2\,\varepsilon + 1 \tag{18}$$

$$\mathscr{N}_{3,3} = -\,(\varepsilon-1)\left(16\,\varepsilon^2\gamma + \varepsilon^2 - 32\,\varepsilon\,\gamma - 2\,\varepsilon + \gamma r^2 + 16\,\gamma + 1\right). \tag{19}$$

For the special case where $c = 0, A = 0$, fixed points can be defined for this system by solving $\mathscr{N}^{-1}\,\boldsymbol{g} = \boldsymbol{0}$. For nonsingular $\mathscr{F}$, this simplifies to $\boldsymbol{g} = \boldsymbol{0}$.

At a fixed point $\dot{\boldsymbol{\xi}} = \boldsymbol{0}$ and $\dot{\delta} = \omega_2 = 0$, requiring that any solution to 5 must result in $\boldsymbol{g} = 0$. Both $\boldsymbol{g}_1 = 0$ and $\boldsymbol{g}_2 = 0$ can be solved by setting

$$\delta^* = \cos^{-1}\left(\frac{\varepsilon\,(\varepsilon-2)}{\varepsilon^2 - 2\,\varepsilon + 1}\right), \tag{20}$$

which gives a turning gait, or

$$\omega_1^* = 0, \tag{21}$$

which results in straight line motion. The equation $\boldsymbol{g}_4 = 0$ is satisfied if $\omega_2 = 0$. The remaining equation $\boldsymbol{g}_3 = 0$ can be satisfied for infinitely many adjacent (u, ω) pairs, resulting in non-isolated fixed points extending away from the constant energy manifold. Evaluating the dynamics reduced to the energy manifold results in isolated fixed points which can then be analyzed for stability. This reduction is performed by defining the system energy

$$E = \mathscr{T}(\boldsymbol{q}, \dot{\boldsymbol{q}}) + \mathscr{V}(\boldsymbol{q}) \tag{22}$$

which, rewritten in $\boldsymbol{\xi}$ coordinates, is

$$E' = \frac{E}{m\,l^2} = \frac{1}{2}\left(u_x^2 + b\,u_x + c\right) \tag{23}$$

for

$$b = m_2'(\varepsilon-1)(\omega_1+\omega_2)\sin\delta \tag{24}$$

$$\tag{25}$$

and

$$c = \left((I_1' + \frac{m_1'\varepsilon^2}{4} + m_2'\varepsilon^2)\omega_1^2 + \left(I_2' + \frac{m_2'(\varepsilon-1)^2}{4}\right)(\omega_1+\dot{\delta})^2 - m_2'(\varepsilon-1)(\omega_1+\omega_2)(\omega_1\,\varepsilon\cos\delta)\right). \tag{26}$$

With energy rescaled, we now once again drop the $'$ superscripts and work only with the rescaled variables. The longitudinal velocity can be written as a function of $(\omega_1, \omega_2, \delta)$ and the energy. The reduced dynamical system is then obtained from the last three equations of (5) where u_x is substituted by a function of the other three state variables, $u_x(\omega_1, \omega_2, \delta; E)$. Suppose $\boldsymbol{H}(\boldsymbol{\xi}) = \mathscr{N}^{-1}\boldsymbol{h}(\boldsymbol{\xi}) \in \mathbb{R}^4$. Setting $\boldsymbol{H}_r(\boldsymbol{\xi}; E) = [\boldsymbol{H}_2(\boldsymbol{\xi}), \boldsymbol{H}_3(\boldsymbol{\xi}), \boldsymbol{H}_4(\boldsymbol{\xi})]^T$, which excludes the first component of $\boldsymbol{H}(\boldsymbol{\xi})$, the reduced dynamical system is

$$\dot{\boldsymbol{\xi}}_r = \boldsymbol{H}_r(\boldsymbol{\xi}_r; E) \tag{27}$$

where $\boldsymbol{\xi}_r = (\omega_1, \omega_2, \delta)$. We then define the fixed points as a function of energy by substituting $u_x(\omega_1, \omega_2, \delta, E)$ into $\boldsymbol{g}_3 = 0$, which gives an expression which can be solved for ω_1^* as

$$\omega_1^* = \pm\frac{\sqrt{2}}{2m_2}\sqrt{A\left(B \pm \sqrt{C}\right)} \tag{28}$$

for

$$\begin{aligned}
A &= \Big(\Big(\varepsilon^2 - \frac{\varepsilon}{2} + \frac{1}{4}\Big)m_2 - \frac{3\varepsilon^2}{4} + I_1 + I_2\Big)((\cos(\delta))^2 - m_2\,\varepsilon\,(-1+\varepsilon)\cos(\delta) + \varepsilon^2)^{-1}(-1+\varepsilon)^{-2}\\
B &= ((-\delta^2\alpha^2 + 2E)\varepsilon^2 + (2\,\delta^2\alpha^2 - 4E)\varepsilon - \delta^2\alpha^2 + 2E)m_2{}^2(\cos(\delta))^2\\
&\quad + (-2\,\alpha^2\delta\,\varepsilon^2 + 4\,\alpha^2\delta\,\varepsilon - 2\,\alpha^2\delta)m_2{}^2\sin(\delta)\cos(\delta) + (4\,\alpha^2\delta\,\varepsilon^2 - 4\,\alpha^2\delta\,\varepsilon)m_2\sin(\delta)\\
C &= (m_2{}^2(-1+\varepsilon)^2\Big(\Big(-\frac{\delta^2}{2} + \delta\Big)\alpha^2 + E\Big)\Big(\Big(-\frac{\delta^2}{2} - \delta\Big)\alpha^2 + E\Big)(\cos(\delta))^2\\
&\quad - 2\,\alpha^2(m_2\,(-1+\varepsilon)(-1/2\,\delta^2\alpha^2 + E)\sin(\delta) - 2\,\alpha^2\delta\,\varepsilon)m_2\,(-1+\varepsilon)\delta\,\cos(\delta)\\
&\quad + 4\,\alpha^2\delta\,(m_2\,(-1+\varepsilon)(-1/2\,\delta^2\alpha^2 + E)\varepsilon\,\sin(\delta) - \alpha^2\delta\,(-1/4\,m_2{}^2(-1+\varepsilon)^2\\
&\quad + (\varepsilon^2 - \varepsilon/2 + 1/4)m_2 + 1/4\,\varepsilon^2 + I_1 + I_2)))(\cos(\delta))^2 m_2{}^2(-1+\varepsilon)^2.
\end{aligned}$$

Through straightforward manipulation of equation 23 we can find

$$u_x = \frac{1}{2}\left(-b \pm \sqrt{b^2 - 4\,(c - 2E)}\right). \tag{29}$$

Substituting $b = b(\omega_1 = \omega_1^*)$ and $c = c(\omega_1 = \omega_1^*)$ into 29 then yields u_x^*.

References

1. L. Meng, R. Kang, D. Gan, G. Chen, L. Chen, D. T. Branson, and J. S. Dai. A mechanically intelligent crawling robot driven by shape memory alloy and compliant bistable mechanism. *Journal of Mechanisms and Robotics*, 12(6), 2020.
2. Y. Tang, Y. Chi, J. Sun, T. Z. Huang, O. H. Maghsoudi, A. Spence, J. Zhao, H. Su, and J. Yin. Leveraging elastic instabilities for amplified performance: Spine-inspired high-speed and high-force soft robots. *Science Advances*, 6(19), 2020.
3. H. Zhang, J. Sun, and J. Zhao. Compliant bistable gripper for aerial perching and grasping. In *2019 International Conference on Robotics and Automation (ICRA)*, pages 1248–1253. IEEE, 2019.
4. G. Wan, Y. Liu, Z. Xu, C. Jin, L. Dong, X. Han, J. X. J. Zhang, and Z. Chen. Tunable bistability of a clamped elastic beam. *Extreme Mechanics Letters*, 34:100603, 2020.
5. A. Cazzolli, D. Misseroni, and F. Dal Corso. Elastica catastrophe machine: theory, design and experiments, 2020.
6. Z. Meng, W. Chen, T. Mei, Y. Lai, Y. Li, and C. Q. Chen. Bistability-based foldable origami mechanical logic gates. *Extreme Mechanics Letters*, 43:101180, 2021.
7. L. L. Howell. *Compliant Mechanisms*. Wiley, New York, 2001.
8. T Greigarn and MC Cavusoglu. Pseudo-rigid-body model and kinematic analysis of mri-actuated catheters. In *2015 IEEE International Conference on Robotics and Automation*, 2015.
9. V. K. Venkiteswaran and H. J. Su. A three-spring pseudorigid-body model for soft joints with significant elongation effects. *Journal of Mechanisms and Robotics*, 8(6), 2016.
10. R. K. Katzschmann, C. Della Santina, Y. Toshimitsu, A. Bicchi, and D. Rus. Dynamic motion control of multi-segment soft robots using piecewise constant curvature matched with an augmented rigid body model. In *2019 2nd IEEE International Conference on Soft Robotics (RoboSoft)*, pages 454–461. IEEE, 2019.
11. H. Zhang, B. Zhu, and X. Zhang. Origami kaleidocycle-inspired symmetric multistable compliant mechanisms. *Journal of Mechanisms and Robotics*, 1(11):011009, 2019.
12. B. Zhu, X. Zhang, H. Zhang, J. Liang, H. Zang, H. Li, and R. Wang. Design of compliant mechanisms using continuum topology optimization: a review. *Mechanism and Machine Theory*, 143:103622, 2020.
13. A. Cazzolli, F. Dal Corso, and D. Bigoni. Flutter instability and ziegler destabilization paradox for elastic rods subject to nonholonomic constraints. 88(3):031003, 2021.
14. S. A. Chaplygin. On the theory of the motion of nonholonomic systems : The reducing multiplier theorem. *Translated version in Regular and Chaotic Dynamics*, 2008.
15. A. V. Borisov and I. S. Mamaev. On the history of the development of the nonholonomic dynamics. *Regular and Chaotic Dynamics*, 7(1):43–47, 2002.
16. A. M. Bloch. *Nonholonomic Mechanics and Control*. Springer Verlag, 2003.
17. S. D. Kelly, M. J. Fairchild, P. M. Hassing, and P. Tallapragada. Proportional heading control for planar navigation: The chaplygin beanie and fishlike robotic swimming. In *Proceedings of the American Control Conference*, 2012.
18. Vitaliy Fedonyuk and Phanindra Tallapragada. Sinusoidal control and limit cycle analysis of the dissipative chaplygin sleigh. *Nonlinear Dynamics*, pages 1–12, 2018.
19. V. Fedonyuk and P. Tallapragada. The dynamics of a chaplygin sleigh with an elastic internal rotor. *Regular and Chaotic Dynamics*, 24(1):114–126, 2019.
20. Chaotic dynamics of the Chaplygin sleigh with a passive internal rotor. V. fedonyuk and p. tallapragada. *Nonlinear Dynamics*, 2018.
21. J. Náprstek and C. Fischer. Appell-gibbs approach in dynamics of non-holonomic systems. In Mahmut Reyhanoglu, editor, *Nonlinear Systems*, chapter 1. IntechOpen, Rijeka, 2018.
22. J. Náprstek and C. Fischer. *Non-holonomic Systems in View of Hamiltonian Principle*, pages 3–25. 01 2021.
23. P. Tallapragada. A swimming robot with an internal rotor as a nonholonomic system. *Proceedings of the American Control Conference*, 2015.
24. P. Tallapragada and S. D. Kelly. Integrability of velocity constraints modeling vortex shedding in ideal fluids. *Journal of Computational and Nonlinear Dynamics*, 2016.
25. B. Pollard, V. Fedonyuk, and P. Tallapragada. Swimming on limit cycles with nonholonomic constraints. *Nonlinear Dynamics*, 2019.
26. J. Lee, B. Free, S. Santana, and D. A. Paley. State-feedback control of an internal rotor for propelling and steering a flexible fish-inspired underwater vehicle. In *2019 American Control Conference (ACC)*, pages 2011–2016. IEEE, 2019.
27. B. A. Free, J. Lee, and D. A. Paley. Bioinspired pursuit with a swimming robot using feedback control of an internal rotor. *Bioinspiration and Biomimetics*, 15(3):035005, 2020.
28. V. Fedonyuk and P. Tallapragada. Path tracking for the dissipative chaplygin sleigh. In *2020 American Control Conference (ACC)*, 2020.
29. L. A. Pars. *A Treatise on Analytical Dynamics*. Ox Bow Press, 1965.
30. A. M. Bloch, P. S. Krishnaprasad, J. E. Marsden, and R. M. Murray. Nonholonomic Mechanical Systems with Symmetry. *Archive for Rational Mechanics and Analysis*, 136:21–99, 1996.
31. A.M. Bloch, M. Reyhanoglu, and N.H. McClamroch. Control and stabilization of nonholonomic dynamic systems. *IEEE Transactions on Automatic Control*, 37(11):1746–1757, 1992.
32. S. K. Soltakhanov, M. P. Yushkov, and S. A. Zegzhda. *Mechanics of non-holonomic systems*. Springer, Berlin Heidelberg, 2009.
33. J. M. Osborne and D. V. Zenkov. Steering the chaplygin sleigh by a moving mass. In *Proceedings of the American Control Conference*, 2005.
34. I. A. Bizyaev, A. V . Borisov, and S. P. Kuznetsov. The chaplygin sleigh with friction moving due to periodic oscillations of an internal mass. *Nonlinear Dynamics*, pages 1–16, 2019.